ARTICLE

Stimuli-Responsive Photoacoustic Nanoswitch for *in Vivo* Sensing Applications

Kenneth K. Ng,[†,⊥] Mojdeh Shakiba,[‡,⊥] Elizabeth Huynh,[‡,⊥] Robert A. Weersink,[⊥,#] Áron Roxin,[§,⊥] Brian C. Wilson,[‡,⊥] and Gang Zheng[†,‡,§,⊥,*]

[†]Institute of Biomaterials and Biomedical Engineering, [‡]Department of Medical Biophysics, [#]Department of Radiation Oncology, and [§]Department of Pharmaceutical Sciences, University of Toronto, Toronto, Ontario M5G 1L7, Canada and [⊥]Princess Margaret Cancer Centre and Techna Institute, University Health Network, Toronto, Ontario M5G 1L7, Canada

ABSTRACT Photoacoustic imaging provides high-resolution images at depths beyond the optical diffusion limit. To broaden its utility, there is need for molecular sensors capable of detecting environmental stimuli through alterations in photoacoustic signal. Photosynthetic organisms have evolved ingenious strategies to optimize light absorption through nanoscale ordered dye aggregation. Here, we use this concept to synthesize a stimuli-responsive nanoswitch with a large optical absorbance and sensing capabilities. Ordered dye aggregation between light-harvesting porphyrins was achieved through intercalation within thermoresponsive nanovesicles. This causes an absorbance red-shift of 74 nm and a 2.7-fold increase in absorptivity of the Q_y-band, with concomitant changes in its photoacoustic spectrum. This spectral feature can be reversibly switched by exceeding a temperature threshold. Using this thermochromic property, we noninvasively determined a localized temperature change *in vivo*, relevant for monitoring thermal therapies of solid tumors. Similar strategies may be applied alongside photoacoustic imaging, to detect other stimuli such as pH and enzymatic activity.

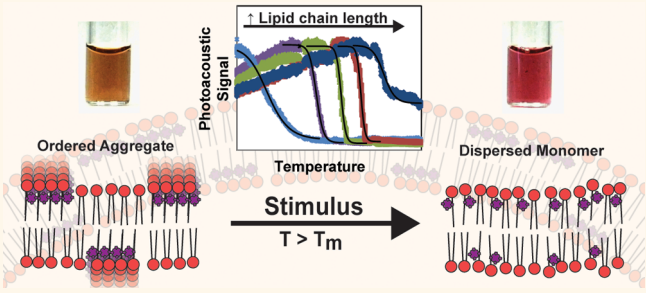

KEYWORDS: nanosensor · stimuli-responsive · phase change material · photoacoustic imaging · J-aggregate · thermochromism

Photoacoustic imaging (PAI) is a hybrid technique that excels at imaging absorbers at depths, that greatly exceed the optical transport mean free path.[1] This is achieved by exciting the target chromophores with nanosecond-pulsed near-infrared light to induce thermoelastic expansion within the tissue. This in turn, generates acoustic pressure waves measurable using a conventional ultrasound transducer.[2] PAI is capable of detecting endogenous absorbers within the body such as hemoglobin, melanin and to some extent, lipids.[3] For this reason, it is useful for examining anatomic and physiological changes that are seen in diseases such as cancer[4,5] and atherosclerosis.[6,7] However, to fully realize the capabilities of PAI for molecular and functional imaging modality, there has been substantial research on exogenous contrast agents such as small-molecule organic dyes,[8] metallic nanoparticles,[9,10] carbon nanotubes[11] and semiconducting polymers[12] compatible with PAI.

As with the advances in fluorescence-based probes,[13] there has been growing interest in stimuli-responsive photoacoustic (PA) nanosensors and switches that are activated in response to biological cues such as the presence of specific enzymes[14,15] or reactive oxygen species.[16] Once activated, these nanosensors typically broadcast their change in state through: (i) altered retention or clearance, (ii) degradation, or (iii) enhancement of nonradiative relaxation of the chromophore. While providing amplification of the input stimulus, these approaches are limited by the activation mechanism being irreversible, which precludes applications involving multiple cycles of activation such as in *in situ* glucose sensing[17] and temperature monitoring during thermal therapy. Hence, a reversible stimuli-responsive PA nanoswitch is required to broaden the purview of PAI.

A class of materials with properties suitable for stimulus sensing are phase change materials.[18] Due to their ability to change

* Address correspondence to gang.zheng@uhnres.utoronto.ca.

Received for review May 26, 2014 and accepted July 21, 2014.

Published online July 21, 2014
10.1021/nn502858b

conformation in response to an external stimuli, phase change materials have been investigated for applications such as, thermal energy storage, information storage and colorimetric temperature sensors. These materials which include saturated phospholipids,[19] liquid crystals,[20] polymers and others have been studied for biomedical applications such as drug delivery.[21]

Photosynthetic organisms have evolved unique mechanisms to optimize and regulate light absorption, through controlled arrangements of dyes within protein and lipid scaffolds.[22] Ordered arrangements between dye molecules can modulate their electronic transitions and induce spectral shifts and changes in optical absorption cross-section.[23] These spectral properties help the organism maximize light collection, as well as provide a gradient for light energy to flow.[24] There have been pursuits to reproduce these pigment−pigment interactions in synthetic nanostructures.[25,26] Discoveries made in the 1930s demonstrated that pseudoisocyanine dyes can form nanoscale aggregates, known as J-aggregates.[27,28] These ordered assemblies display a large, red-shifted absorbance owing to interactions between the transition dipoles of adjacent dyes[29] and have been studied as synthetic models of light harvesting antennae.[30] Other dyes have also been discovered to behave similarly.[31−33] Given the noncovalent interactions that govern the coupling between dyes and the conformation-dependent changes in absorption spectra, these ordered dye aggregates have potential as stimuli responsive PA nanoswitches. Here, we utilize reversible coherent dye aggregation to build a novel stimuli-responsive PA nanoswitch with controllable spectral characteristics. We show that these nanoswitches can modulate the PA signal when a predefined temperature is exceeded and explore their utility as temperature sensors in thermal therapy.

RESULTS AND DISCUSSION

Bacteriochlorophyll *a* is known to form circular homomeric dye aggregates within the light harvesting complex of various photosynthetic purple bacteria.[23,34] Edge-to-edge packing of the dye molecules in this ring is facilitated by the rigid environment of the light harvesting complexes protein scaffold and surrounding lipid membrane. We reasoned that by conjugating this light-absorbing moiety to a phospholipid tail and intercalating it into a lipid matrix, it would be possible to induce the ordered arrangement and a resulting change in the dye's absorption spectrum. Indeed, previous studies have shown that planar organic dyes from the cyanine[35,36] and porphyrin[37,38] families of molecules can form ordered J-aggregates within amphipathic membranes.

Bacteriochlorophyll *a* was isolated from *Rhodobacter sphaeroides* and processed to generate bacteriopheophorbide *a* (Bchl),[39] which was then conjugated to 1-palmitoyl-2-hydroxy-*sn*-glycero-3-phosphocholine to form bacteriopheophorbide *a*-lipid (Bchl-lipid)[40] (Figure 1A). We prepared lipid films by mixing dipalmitoylphosphatidylcholine (DPPC) and 1,2-dipalmitoyl-*sn*-glycero-3-phosphoethanolamine-*N*-[methoxy(polyethylene glycol)-2000] (mPEG2000-DPPE) and Bchl-lipid at a dye-to-total lipid ratio of 15 mol % and prepared vesicles by freeze−thaw extrusion. Transmission electron microscopy showed that the nanoparticles thus formed have a spherical vesicle structure (Figure 1B). During formulation, the sample color varied with the temperature of the solution, changing from dark brown to bright pink when heated (Figure 1B). Absorption spectroscopy of the extruded sample at room temperature showed a 74 nm red-shift in the Q_y absorbance transition to 824 nm when compared to the detergent solubilized sample (Figure 1C) or the monomeric dye (Supporting Information Figure S2). The molar absorption coefficient of the Q_y absorbance transition at 824 nm was found to be 1×10^5 cm^{-1} M^{-1}, which is 2.7-fold higher than the Q_y transition of Bchl-lipid dissolved in methanol. Furthermore, the full width at half-maximum (fwhm) of the Q_y absorption band was smaller (25 nm) than that of the monomeric dye solubilized in methanol (44 nm). This exchange-narrowing phenomenon is a known property of coherently coupled J-aggregates.[41] In addition, compared with Figure 1C, the fluorescence spectra showed a characteristic negligible Stokes shift, further evidence of J-aggregate formation (Figure 1E).[27] Circular dichroism (CD) spectrophotometry, which provides information on both intra- and intermolecular chirality, demonstrated that the sample adopts a negative Cotton effect peak near the Q_y absorption maximum, while addition of the detergent, Triton X-100, eliminates the peak (Figure 1D). This indicates ordered chiral packing of Bchl-lipid molecules in the nanovesicle membrane.

J-aggregation of Bchl was found to occur only for dyes conjugated to lipids and not with unconjugated dye embedded in the membrane. Loading Bchl at 15 mol % into a lipid vesicle resulted in a moderate red-shift in the Q_y-absorbance to 796 nm, but the peak was broadened compared with the monomeric spectrum (fwhm = 80 nm), indicating disordered aggregation (Supporting Information Figure S3). These results suggest that the aggregates formed by Bchl in nanovesicles differ from those formed from Bchl-lipid. Taken together, these properties support the conclusion that coherently coupled Bchl-lipid molecules form J-aggregates in the nanovesicle membrane, hereafter referred to as J-aggregating nanoparticles (JNP).

We were interested in determining whether Bchl-lipid was stably inserted into the nanovesicle membrane and whether there was the possibility of lipid exchange occurring between liposomes. To test this, we studied the effect of mixing JNP, prepared with

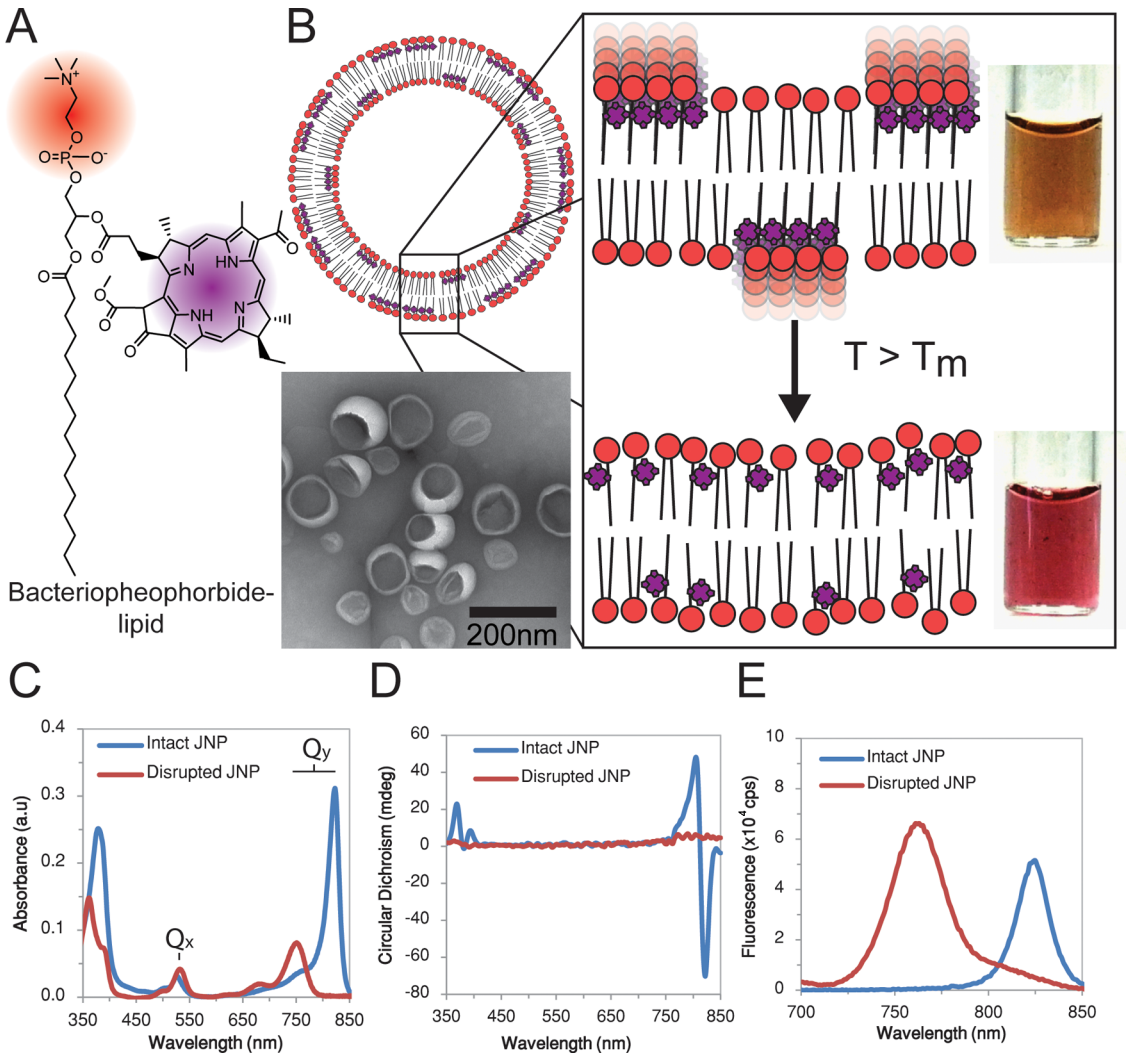

Figure 1. (A) Structure of bacteriopheophorbide-lipid with axes showing the Q_y and Q_x transition dipoles for the chromophore. (B) Schematic of the J-aggregating nanoparticle (JNP) prepared with 15% Bchl-lipid, 80% host phospholipid, and 5% mPEG2000-DPPE. Insets: (left) Representative transmission electron micrograph of JNP prepared with dipalmitoyl-phosphatidylcholine (DPPC) (JNP16) and (right) color photographs of JNP16 sample below and above phase transition temperature. (C) Absorption spectra of JNP16 in the intact (blue) and detergent disrupted (red) state. (D) Circular dichroism spectra of JNP16 in the intact (blue) and detergent disrupted (red) state. (E) Fluorescence spectra of JNP16 in the intact (blue) and detergent disrupted (red) state.

dipalmitoylphosphatidylcholine (DPPC) (JNP16) with unlabeled DPPC liposomes and measured the extent of Bchl-lipid transfer between nanoparticles by measuring changes in J-aggregate or monomeric Bchl-lipid fluorescence. If lipid transfer occurred during incubation, we should expect a fluorescence wavelength shift from 824 nm (aggregate emission) to 750 nm (monomer dye emission) due to the transfer of individual dye molecules to the unlabeled liposomes. Upon mixing JNP16 with up to a 10-fold mol (total lipid) excess of liposomes, we observed a small increase in fluorescence at 750 nm over a period of 24 h (Supporting Information Figure S4A). This indicated that lipid exchange occurs between liposomes. Interestingly, we did not observe any significant changes in the fluorescence spectra at 824 nm (Supporting Information Figure S4B), nor the absorbance spectra of JNP16 over the same time period (Supporting Information Figure S4C,D). This demonstrated that there was minimal Bchl-lipid exchange occurring between liposomes and transfer did not affect the absorbance properties of the nanovesicle. We were also interested to test whether insertion of Bchl-lipid into the liposome structure promoted instability in JNP16. We prepared and stored JNP16 at 4 °C at a concentration of 50 μM in PBS over 7 days (Supporting Information Figure S5). Over this time period, we did not observe any aggregation induced increases in liposome size.

Next, the effect of temperature-induced changes in membrane fluidity on J-aggregates was investigated. The absorbance of JNP16 was measured as a function of temperature (Supporting Information Figure 2A). With increasing temperature, a decrease in the J-aggregate

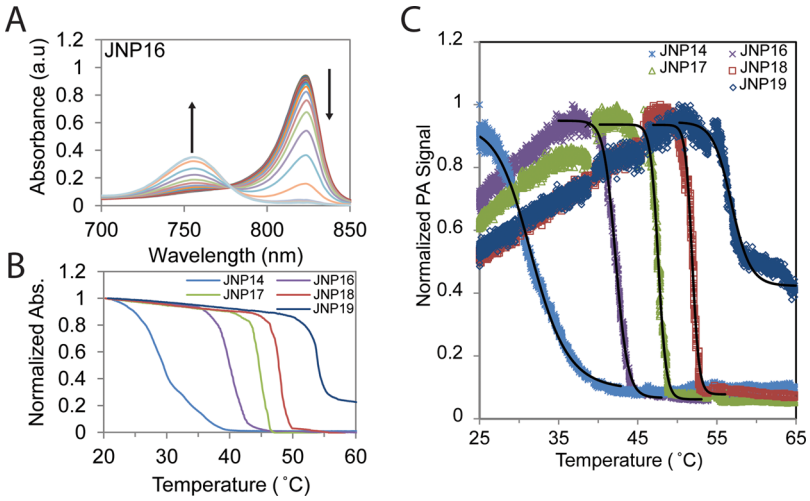

Figure 2. UV/visible absorbance melt curves for JNP prepared with host phospholipids with varying acyl chain lengths. (A) Representative near-infrared absorption spectrum of JNP prepared with dipalmitoylphosphotidylcholine (JNP16) upon heating from 25 to 50 °C. (B) The effect of heat on the 824 nm absorption of JNP prepared with dimyristoylphosphocholine (JNP14), dipalmitoylphosphotidylcholine (JNP16), diheptadecanoylphosphotidylcholine (JNP17), distearoylphosphotidylcholine (JNP18). and dinonadecanoylphosphotidylcholine (JNP19). (C) The effect of heat on the normalized PA signal amplitude of JNP14, JNP16, JNP17, JNP18. and JNP19.

absorption at 824 nm was observed, together with an increase in the monomeric absorption of the dye at 750 nm. This effect was most pronounced near the phase transition temperature of the host lipid (41 °C). In addition, observation of both the fluorescence emission (Supporting Information Figure S6A) and circular dichroism of JNP16 (Supporting Information Figure S6B) below and above the phase transition temperature showed a conversion from the aggregate to monomeric population of dyes. Thermal energy can have two distinct effects on this nanoparticle system, which together explain the decrease in absorbance with increasing temperature. The first effect is an increase in the vibrational mobility of the Bchl-lipid dyes that causes small changes in the dye arrangement and a weakening of the molecular coupling. The second effect is a change in phase behavior of the host lipid, which confers fluidity to the entire membrane. This significantly increases the translational mobility of Bchl-lipid in the membrane, promoting physical separation of the dye molecules. Hence, near the transition temperature of the host lipid, an initial weakening of the interactions between Bchl-lipid molecules followed by increased translational mobility in a more fluid membrane results in a large decrease in J-aggregate absorbance. On the other hand, when Bchl alone was embedded in the DPPC phospholipid membrane, the decrease in absorption in heating from 20 to 50 °C was only 15% (Supporting Information Figure S3), compared to a 99% decrease observed in nanovesicles prepared with Bchl-lipid (Figure 2B). These data suggest that the aggregates formed by the self-association of Bchl are not affected by the increased membrane fluidity resulting from phase change of the host phospholipid. Using phospholipids with an increasing number of carbons in the fatty acid tail [dimyristoylphosphocholine (JNP14), dipalmitoylphosphotidylcholine (JNP16), diheptadecanoylphosphotidylcholine (JNP17), distearoylphosphotidylcholine (JNP18) and dinonadecanoylphosphotidylcholine (JNP19)], we found that the midpoint of the temperature melt curve can be varied with the length of the phospholipid acyl chain (Figure 2B). This suggests that the physical state of the host phospholipid plays a critical role in dictating the ordered arrangement of the Bchl-lipid molecules and that nanosensors can be created and tuned to respond over a broad range of thermal thresholds.

Given this heat-induced change in the nanoparticle absorbance, the utility of JNP as a photoacoustic (PA)-based temperature sensor was investigated. Looking at the PA signal at 824 nm as a function of temperature (Figure 2C), we observed an initial increase in PA signal. This was expected, given the direct relationship between temperature and the Grüneisen parameter.[42,43] However, when the sample was heated beyond the transition temperature of its host phospholipid, a rapid decrease in PA signal was observed, corresponding to the absorbance melt curves (*vide supra*). The photoacoustic spectrum of each sample prior to heating and after heating showed spectral features consistent with measurements made using UV/Visible spectroscopy (Supporting Information Figure S7)

We also observed that disaggregation of Bchl-lipid molecules in JNP16 with increasing temperature was reversible and the phase transition temperature midpoint remained the same during 5 successive heating−cooling cycles, showing the robustness of the system. The temperature hysteresis observed during successive cooling cycles can potentially be explained by the required time for the monomers to reassemble into coherently coupled domains (Figure 3A).

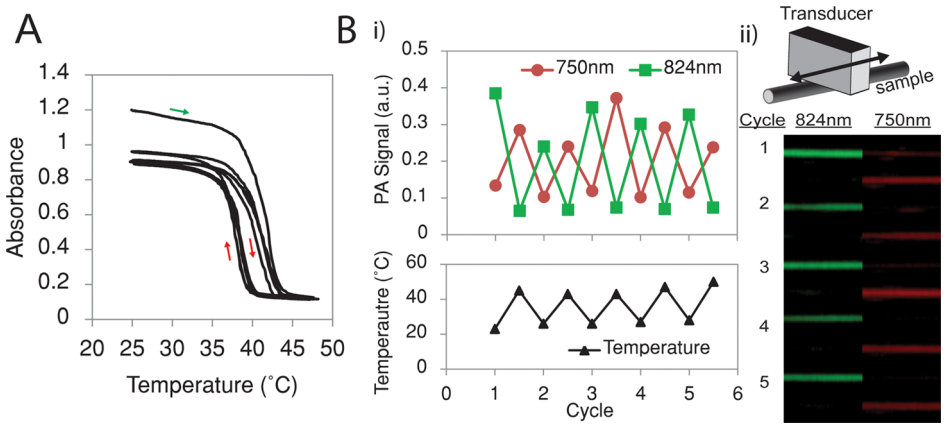

Figure 3. Reversibility of JNP absorption and photoacoustic signal during thermal cycling events. (A) Temperature cycling of JNP16 while monitoring the absorbance at 824 nm. (B) Reversibility in PA signal at 824 nm during heating cycles above and below JNP16's phase transition midpoint: (i) the temperature was raised and cooled during each cycle and the PA signal at 824 nm (green) and 750 nm (red) were recorded; (ii) reconstructed 3D PA projection image of JNP16 sample during consecutive thermal cycles. Schematic shows placement of PA transducer and sample-filled polyethylene tubing for image acquisition.

To assess this hypothesis, isothermal experiments (at 25 °C) conducted on JNP16 after a brief 15 min incubation above its phase transition temperature showed the J-aggregate absorption band of the heated sample slowly recovers with time (Supporting Information Figure S8). Studies conducted on various types of phospholipids have demonstrated the existence of additional metastable phases which exist below the gel → liquid phase transition temperature.[44] These metastable phases can form upon cooling, but may be distinct from the equilibrium state. Depending on the composition of the system, these metastable phases can exist over a wide range of time scales. It is possible that Bchl-lipid forms a metastable phase upon cooling, which gradually reaches its final equilibrated state after prolonged incubation or storage. Since the intensity of the absorption band is dependent on the relative conformation of adjacent dye molecules, which in turn is dependent on bilayer packing, small changes in conformation can cause large changes in absorption.

Repeated heating–cooling cycles also resulted in similarly periodic changes in PA signal intensity at 824 nm (Figure 3B), and a decrease in the signal at 824 nm coincides with an increase in the monomeric signal at 750 nm. Taken together, these data suggests that the temperature threshold sensing capability is reversible and can be repeated over several heating–cooling cycles.

The ability to determine the spatial extent of heating in tissue during thermal therapy is of critical importance, since it can guide heat delivery to maximize therapeutic efficacy while minimizing damage to adjacent healthy tissue. Due to unknown heterogeneity in tissue composition and blood flow, it is difficult to accurately model heat distribution during therapy. Given the ability of JNP to sense thermal thresholds *via* a decrease in PA signal, we tested the capability to generate temperature threshold maps to track heat delivery. Three-dimensional scans using PA imaging can be easily obtained with a 1-D linear transducer array scanning along one axis. When these imaging capabilities are combined with the temperature threshold sensing abilities of JNP, temperature threshold maps can be generated to track heat delivery. For proof-of-principle, a solution of JNP16 nanoparticles was embedded within a polyacrylamide gel phantom and the PA signal of the sample was monitored during heating (Figure 4A). Thermal images of the sample were simultaneously obtained using an infrared camera (Figure 4A). During the course of heating, the progression of the thermal front could be seen as a region of diminishing signal at 824 nm. An increase in signal at 750 nm in the same region showed that the signal decrease at 824 nm is a result of disaggregation of Bchl-lipid molecules and is not due to movement of the nanoparticles out of the imaging plane. The thermal front determined by PA imaging (as a decrease in intensity at 824 nm) was found to correlate with the temperature front that exceeded 41 °C in the infrared images (R^2 = 0.92), thus demonstrating the ability of PA imaging with JNP-based contrast to map temperature thresholds during thermal therapy in real-time (Figure 4B).

As a proof-of-principle, JNP-based PA temperature sensing *in vivo* was tested in a murine tumor xenograft. KB-tumor bearing mice were intratumorally injected with saline, JNP16 (130 μM), or indocyanine green (ICG; 130 μM) and immobilized in a custom-built water bath. The temperature was then increased from 25 to 52 °C, while a PA transducer in contact with the tumor collected images at 680, 750, 800, 824, and 850 nm. As expected, animals injected with saline did not display any enhancement in the 824 nm signal, while blood in the tumor could be visibly observed at 680 nm (Figure 5A; Supporting Information Video 1).

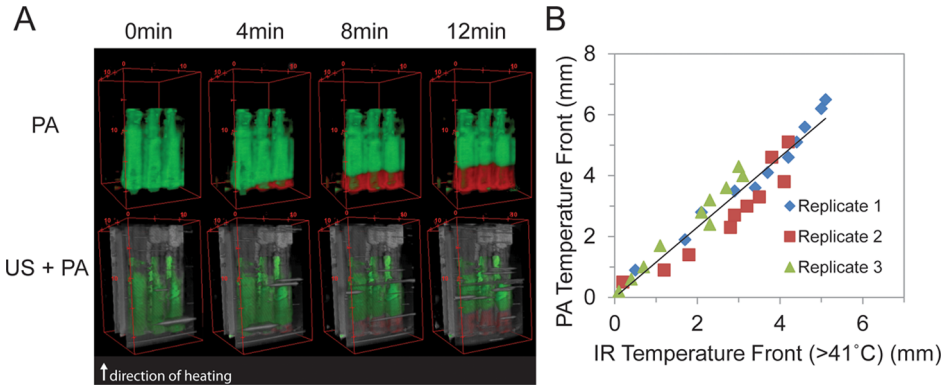

Figure 4. Temperature response of JNP16 loaded into polyacrylamide gel phantom during heating. (A) PA and US images at various times during heating: PA signal at 750 nm (red) and 824 nm (green). The gradations along the bounding wireframe shows the dimensions of the gel (in mm). (B) Correlation between the thermal front (>41 °C) determined from infrared thermography and from PA imaging (amplitude decrease at 824 nm).

Tumors injected with JNP16 showed marked 824 nm PA signals originating from at the center of the tumor (Figure 5B; Supporting Information Video 2) that were clearly visible over the blood background at this near-infrared wavelength where hemoglobin absorption is low. Heating the tumor produced an initial increase in the Q_y-band signal, followed by a 2.7-fold decrease in the intensity. The midpoint of the observed transition temperature was 44 °C. This PA signal profile differed from the ICG-injected tumors, which showed the initial signal increase but this then did not disappear upon exceeding 40 °C (Figure 5C; Supporting Information Video 3). These results demonstrate that the temperature-threshold sensor works even in a complex *in vivo* tumor setting. The discrepancy between the measured phase transition temperature in the tumor and that measured in the solution experiments is due to the temperature lag between the water bath and the intratumor environment caused by the insulating and heat-sinking effects of the intervening tissue. This was confirmed by placing thermocouples both in the water bath and interstitially at a depth of 2 mm into the tumor to directly monitor the temperatures. As shown in Supporting Information Figure S10, the average temperature difference was 2.0 $\pm$ 0.5 °C, which is consistent with the apparent discrepancy in the phase transition temperature.

The ability to resolve images at significant depths in tissue is one of the advantages of PA imaging over other optical techniques with similar resolution.[1] However, sensitivity remains a challenge, since the signal from tissue is generally weak and of low contrast in the absence of blood vessels. This can be addressed by the use of exogenous contrast agents. While gold nanoparticles[45] and single-walled carbon nanotubes[11] provide significant enhancements in optical extinction, other materials[14,28] have generated excitement, due in part to their ability to produce functional information using PAI.[16,40] JNP have favorable spectral characteristics which lend its utility in PAI. The coupling of the transition dipoles of embedded dyes within the nanovesicle structure causes a large (74 nm) red-shift of the Q_y absorption to 824 nm. At this wavelength, the blood absorption is low, so there is minimal background in the images. Combined with the narrowing of the absorption band, these properties enable effective spectral unmixing and potential multiplexing with other exogenous agents. Additionally, due to the conformational lability of the dye aggregates, a sensing system (*e.g.*, thermoresponsive phospholipids) that reversibly modulates the conformational state of the aggregates could be devised for *in vivo* sensing applications.

Our design of a nanoparticle switch to visualize temperature thresholds in real-time is fundamentally different from existing PA-based temperature sensing techniques. While several groups have utilized the temperature-dependence of the Grüneisen parameter to measure tissue temperature,[43,46−48] clinical application of this approach is hindered by the need to calibrate each tissue type. Furthermore, the need to acquire background images for subtraction from the contrast image makes it prone to motion artifacts. Recently, this problem was elegantly tackled by Yao and colleagues, who demonstrated the feasibility of making absolute PA temperature measurements[49] by first measuring the Grüneisen-dependent PA amplitude and the speed of sound in the tissues, and then applying a ratiometric measurement at two separate temperatures. In the case of JNP sensors, the temperature sensing mechanism is an intrinsic physical property of the nanoparticle, which eliminates the need for baseline measurements or calibration in control tissues. Furthermore, since the nanoparticle is designed to report a specific and selectable temperature threshold, the measurement is direct and tissue-independent. Additionally, this method is independent of the local concentration of the nanovesicles as long as there is adequate PA signal from the particles over the tissue background.

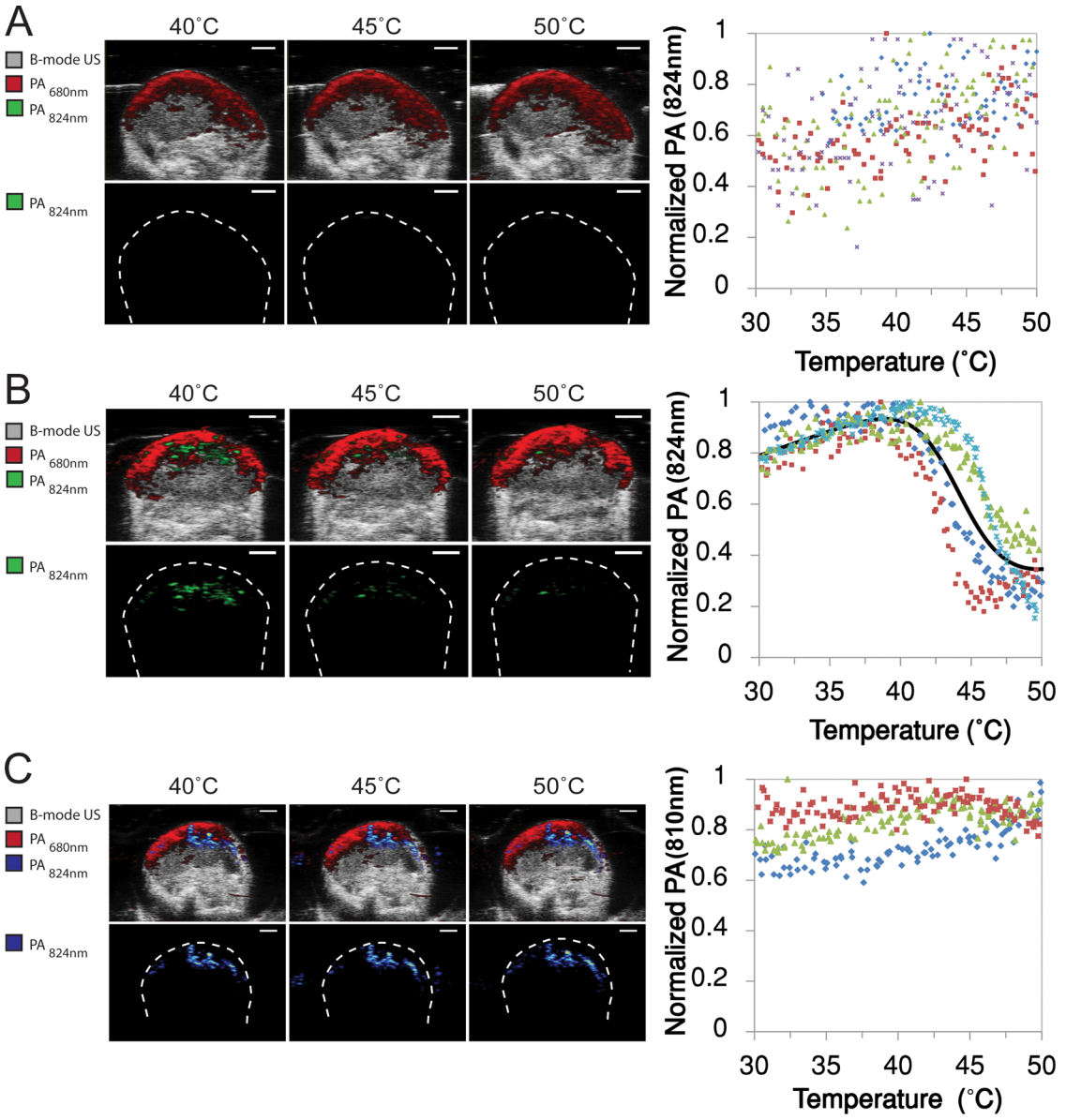

Figure 5. Temperature threshold sensing in tumor xenografts. All image panels show representative images of tumors at 40, 45, and 50 °C with the top row showing the ultrasound, PA680 (hemoglobin) and PA824/810 (JNP/ICG). The bottom row shows the contrast agent signal (PA824/810) alone for clarity. The scale bar in each image corresponds to 2 mm. (A) PA images (λ = 680 and 824 nm) of tumors injected with saline (left) and a PA-temperature plot showing the influence of heating on PA signal (each color represents the data from 1 animal, n = 4) (right). (B) PA images (λ = 680 and 824 nm) of tumors injected with 130 μM JNP16 (left) and a PA-temperature plot showing the influence of heating on PA signal (each color represents data from 1 animal, n = 4) (right). (C) PA imaging of tumors (λ = 680 and 810 nm) injected with 130 μM indocyanine green (left) and a PA-temperature plot showing the influence of heating on PA signal (each color represents data from 1 animal, n = 4) (right).

There are some limitations to this strategy for sensing temperature which have yet to be resolved. First, as with any contrast agent, the signal generated is related to the local concentration of the agent at the imaging site. A general challenge for contrast agents and especially with nanoparticles is the influence of tumor heterogeneity on blood flow. This can affect contrast enhancement in the tumor and hence the sensing capability of JNP. Despite the capability of accumulating in tumors through the enhanced permeation and retention effect, the spatial deposition of nanoparticles will be dictated by the distribution of blood vessels within the tumor. The extent that inter- and intratumor heterogeneity influences the enhanced permeation and retention effect has yet to be resolved.[50] Second, compared to other techniques, this method can only measure binary changes in tissue temperature as manifested in threshold changes in photoacoustic signal. As such, this technique will be more useful for applications where it is not necessary to measure a broad range of tissue temperatures. An example of this is in tissue ablation, where it is only necessary to determine whether tissue temperature has exceeded the tissue coagulation threshold.

CONCLUSION

In summary, we show that ordered aggregates of coherent coupling Bchl-lipid dyes can be formulated into stimuli responsive PA nanoswitches. For the particular application of thermal therapy monitoring and guidance, we show that, by embedding the dyes in a temperature sensitive nanovesicle with a defined phase transition temperature, we can detect threshold changes in temperature. The large absorption caused by coupling of dye aggregates provides contrast enhancement in tissues, while the conformational lability of the dye aggregates confers temperature threshold sensing. Furthermore, by varying the host phospholipid chemical structure, a range of temperature thresholds can be measured that allows for tailoring to specific temperature-related applications. Used in conjunction with PAI, a spatial map of the temperature threshold can be generated and it correlates well with temperatures monitored by thermographic imaging. Lastly, we have demonstrated that JNP can detect tissue temperature thresholds upon injection into murine tumor xenografts subjected to tissue heating, despite the presence of other endogenous optical absorbers. While temperature was the specific biological stimuli monitored with these nanoparticles, the concept of using reversible intermolecular dye coupling to report changes in wavelength and intensity can be extended to other stimuli such as pH and enzymatic activity.

METHODS

Materials. Dimyristoylphosphotidylcholine (DMPC), dipalmitoylphosphatidylcholine (DPPC), diheptadecanoylphosphotidylcholine (DHPC), distearoylphosphotidylcholine (DSPC), dinonadecanoylphosphotidylcholine (DNPC), 1-palmitoyl-2-hydroxy-*sn*-glycero-3-phosphocholine, and 1,2-dipalmitoyl-*sn*-glycero-3-phosphoethanolamine-*N*-[methoxy(polyethylene glycol)-2000] (PEG2000-DPPE) were purchased from Avanti Polar Lipids, Inc. (Alabaster, AL) and reconstituted with chloroform prior to use. Polyethylene tubing with (1.09 mm internal diameter) was purchased from Becton Dickinson and Company (Sparks, MD) and was thoroughly washed with ethanol before use. Extruder drain discs and polycarbonate membranes were purchased from Whatman (Piscataway, NJ). Polyacrylamide was purchased from Bio-Rad (Mississauga, ON).

Synthesis of Bacteriopheophorbide *a*-Conjugated Lipid. Bacteriopheophorbide *a*-conjugated lipid (Bchl-lipid) was synthesized as previously reported.[40] Briefly, bacteriopheophorbide *a* (100 mg, 163.7 μmol, 1.0 equiv), 1-palmitoyl-2-hydroxy-*sn*-glycero-3-phosphocholine (106.8 mg, 215.5 μmol, 1.3 equiv), 1-ethyl-3-(3-dimethylaminoporpyl)carbodiimide hydrochloride (36.6 mg, 190.9 μmol, 1.17 equiv), and *N*,*N*-dimethylaminopyridine (60 mg, 491.1 μmol, 3.0 equiv) were dissolved in 5 mL of anhydrous $CHCl_3$ (amylene stabilized). The vessel was sealed with a rubber septum, and the solution was purged with Ar(g) for 2 min. The vessel was protected from light, and the solution was stirred at room temperature for 5 days. The crude was then purified using a diol silica gel (16 g) column while eluting byproducts using DCM, bacteriopheophorbide *a* using DCM with 1% MeOH (v/v), and the Bchl-lipid product using DCM with 3% MeOH (v/v). The collected fraction was concentrated using rotary evaporation. The concentrated solution was used to quantify the yield of Bchl-lipid spectrophotometrically and to characterize the purity of the product using HPLC–MS analysis. HPLC–MS showed that 3 isomers of Bchl-lipid were made (1:2:0.25 ratio), each with identical absorbance spectra and mass spectra (Supporting Information Figure S1). These procedures yielded 63.6 mg (58.5 μmol) of Bchl-lipid (36% yield). The product was then dried using rotary evaporation and was further dried in a vacuum chamber overnight. The purified Bchl-lipid was finally stored under Ar(g) at −20 °C. ESI + MS: $[M + 1]^+ = 1089$ *m*/*z*. UV–vis (MeOH, λ_{max}): 747, 526, 358 nm.

Synthesis of JNP. Bchl-lipid containing JNP were made by the freeze–thaw extrusion technique as previously described.[40] Briefly, 15 mol % Bchl-lipid, 5 mol % mPEG2000-DPPE, and 80 mol % host lipids (either DMPC, DPPC, DHPC, DSPC, or DNPC) dissolved in chloroform were transferred to borosilicate glass tubes and dried by N_2 to form a thin film. The film was then transferred to a vacuum desiccator and dried for an additional 30 min to ensure complete solvent removal. Films were hydrated with PBS, subjected to 10 freeze–thaw cycles, and extruded through 100 nm polycarbonate membranes using a hand extruder or a high pressure extruder set to a temperature of 70 °C. Prepared samples were stored at 4 °C until used. Control samples were prepared in the same way as above with the exception that Bchl was substituted in place of Bchl-lipid.

Characterization of JNP. *UV/Visible Absorption Measurements.* UV/visible absorption spectra of JNP were measured in PBS using a Cary 50 UV–visible spectrophotometer (Agilent, Mississauga, ON). The concentration of Bchl-lipid from each JNP sample was determined in methanol using the molar absorption coefficient of 37 000 M^{-1} cm^{-1}. Measurement of absorption spectra of detergent disrupted samples was conducted by diluting samples in Triton X-100 such that the final concentration of detergent was (0.1% v/v)

Fluorescence. Fluorescence measurements were carried out on a Fluoromax-4 spectrofluorometer (Horiba Jobin Yvon, NJ). JNP samples were diluted such that the Bchl-lipid concentrations in all solutions were equal. Measurements comparing the intact and detergent disrupted JNP were made by using a 520 nm excitation wavelength (2 nm slit width), while the emission spectrum was scanned from 700 to 900 nm (2 nm slit width). Measurement of fluorescence spectra from detergent disrupted samples was conducted by diluting samples in Triton X-100 to a final concentration of 0.1% v/v.

Circular Dichroism. Circular dichroism (CD) measurements were made using a temperature-controlled Jasco J-815 CD spectrophotometer (Jasco, Easton, MD). CD spectra were collected by scanning from 350 to 850 nm in 1 nm increments.

Dynamic Light Scattering. Dynamic light scattering measurements were made using a Zetasizer ZS90 (Malvern Instruments Ltd., Malvern, U.K.). JNP samples were sized immediately after extrusion as well as after storage for 1 week at 4 °C

Transmission Electron Microscopy. Transmission electron microscopy was carried out on a Hitachi H-7000 electron microscope with an acceleration voltage of 75 kV. Ten microliters of sample was applied to a glow-discharged 200-mesh copper-coated grid. The sample was washed twice with 30 μL of ddH_2O and stained with 2% (w/v) uranyl acetate.

Absorbance–Temperature Profiles. Absorbance–temperature profiles were collected on the temperature controlled Jasco J-815 CD spectrophotometer. Measurements were subtracted from baseline measurements using PBS at 824 nm. A thermocouple was inserted into the cuvette for monitoring temperature. The temperature within the sample cell was gradually heated from 20 to 60 °C at 5 °C min^{-1} with absorbance measurements made every 0.1 °C. Temperature cycling experiments were conducted as described above with ramp temperatures set from 25 to 60 °C at a rate of 5 °C min^{-1} for both the heating and cooling steps.

Lipid Exchange between JNP and Unlabeled Liposomes. JNP16 was prepared along with control DPPC liposomes

containing 5% mPEG-DPPE lipid. The control liposomes, prepared at 5 mM (total lipid), were made using the same method which involved freeze–thaw and extrusion through 100 nm pore polycarbonate membranes. JNP16 was incubated at room temperature with the control liposomes at various ratios such as 2:1, 3:1, 4:1, 5:1, 10:1 (DPPC liposomes mol/JNP16 mol). Absorbance and fluorescence measurements were acquired using the CLARIOstar microplate reader (BMGtech, Offenberg, Germany). Measurements were made immediately after mixing, as well as 17 and 24 h after incubation. For absorbance measurements, spectral scans of each well were acquired in 2 nm increments from 400 to 850. For fluorescence measurements, the excitation bandpass was set to 525 nm with a bandwidth of 16 nm. This region of the spectrum corresponds to a near equal absorbance in the monomeric and the aggregate absorption. The fluorescence emission was collected at 760 or 825 nm, both with a 10 nm bandpass.

Storage Stability of JNP. JNP prepared in PBS at a concentration of 50 μM with methods described above were stored at 4 °C over the course of the experiment. Immediately after formulation (0 h), 1 day, 3 day, and 7 day postformulation, the JNP were sized and the volume size distribution was recorded.

Photoacoustic Signal–Temperature Profiles. Photoacoustic imaging was performed using a Vevo 2100 LAZR photoacoustic imaging system (Fujifilm, Toronto, ON) equipped with a 21 MHz-centered transducer and a flashlamp-pumped 20 Hz Q-switched Nd:YAG laser, tunable from 680 to 970 nm with a 2 nm step size. Photoacoustic-temperature profiles were collected in a custom-built heating apparatus composed of 5 polyethylene tubes fixed within a plastic holder. The tubes loaded with JNP prepared with host phospholipids of various acyl chain lengths were submerged in the holder in a glass beaker filled with degassed water and a stir bar. The photoacoustic transducer was placed such that the ultrasound array captured an image slice through each tube. The temperature in the bath was increased from 25 to 60 °C using a hot plate while it was monitored using a thermocouple placed in the same depth of water as the plastic tubing. Data from each plot were curve fitted with a 4-parameter logistical equation using Sigma-Plot (Systat Software, Inc. San Jose, CA).

Photoacoustic Imaging in Gel Phantoms. *Gel Phantom Preparation.* Polyacrylamide photoacoustic hydrogel phantoms were prepared using the method described by Choi and colleagues[51] with modification. Briefly, 59 mL of ddH_2O, 30 mL of 30% (w/v) 19:1 acrylamide, and 10 mL of 1 M Tris buffer (pH 8) were combined in an Erlenmeyer flask and degassed under vacuum for 15 min. Ammonium persulfate (APS; 10% w/v) and *N*,*N*,*N*′,*N*′-tetramethylethylenediamine (TEMED) were added to the monomer solution to final concentrations of 0.84% and 0.2%, respectively. Polymerizing solution was rapidly poured into a custom built rectangular gel mold and comb and allowed to polymerize for 1 h. The monomer solution was prepared once again; however, a volume of the ddH_2O was replaced with a solution of JNP such that the final JNP concentration was 30 μM. Once the outer gel was polymerized, the comb was removed and the empty space was filled with the newly prepared JNP gel solution. Gels were used immediately after polymerization.

Imaging Conditions and Procedures. Photoacoustic imaging was performed using the photoacoustic imaging system as described above. Hydrogel phantoms were placed on a resistive heating element (20 V; 25 cm^2; McMaster-Carr; cat# 35475K263) to provide heat to the JNP filled gel. PA images were collected on the gel phantom during the experiment by aligning a 21 MHz transducer array parallel to the direction of heating and scanning across the gel to generate a 3D image of the gel. The excitation wavelength was alternated between 750 and 824 nm during the scan. While the gel images were scanning, thermographic images were captured using an infrared camera placed perpendicular to the direction of heating.

Image Processing. Thermographic images were analyzed using Mikrospec 4.0 imaging software. All other analysis was conducted using ImageJ. The thermal front exceeding 41 °C in the hydrogel phantom was measured and compared with the thermal front determined from the decrease in signal intensity at 824 nm. The data were fitted using linear least-squares regression through the origin.

Measurement of Photoacoustic Signal–Temperature Profiles in Tumor Xenografts. All animal procedures were approved and conducted in accordance with University Health Network's Animal Research Committee.

Tumor Inoculation. KB cells were cultured in Eagle's Minimum Essential Medium supplemented with 10% fetal bovine serum. Immediately prior to tumor inoculation, KB cells were trypsinized and washed 3 times with phosphate buffered saline. The concentration of cells was adjusted to 2×10^7 cells/mL and kept on ice throughout the experiment. Animals were anesthetized with a gaseous mixture of isofluorane and oxygen. Once induction of anesthesia was complete, the hind flank of each animal was inoculated with 2×10^6 cells.

Imaging Conditions and Procedures. Heating experiments were conducted to test the effect of heating on the signal change of JNP once tumors reached an appropriate size (average volume = 263 mm^3). Anesthetized animals were placed on a stage in the PA imager. The hind limb was immobilized in a temperature-controlled water bath (Supporting Information Figure S9). The temperature in the bath was slowly raised during the heating procedure (average heating rate = 1.8 °C/min) and monitored using a thermocouple. Animals were split into three groups each receiving 100 μL of saline (n = 4), JNP16 (130 μM; n = 4), or indocyanine green (130 μM; n = 4) delivered through a 21G needle inserted 2 mm below the surface of the tumor. Immediately after injection, the 21 MHz PA transducer was placed on the tumor and images were collected throughout the heating procedure. The water bath temperature was increased from 25 to 50 °C while the ultrasound and PA images were collected. For PA imaging, the excitation laser wavelength was cycled sequentially between 680, 750, 800, 824, and 850 nm. To determine the extent of a temperature differential in the water bath *versus* within the tumor, thermocouples were inserted in the water bath and tumor, with tip buried 2 mm below the surface of the tumor. Heating of the tumor was conducted as above. The water bath and tissue temperatures were compared, and the difference between the two was calculated for each temperature point.

Image Processing. To quantify the PA signal arising from the JNP as a function of temperature, regions of interest were drawn around the center of the tumor for each animal. The signal at each of the 5 wavelengths was plotted against the water bath temperature by matching the PA image time with the thermocouple measurement time. The PA signal at 850 nm was used as a baseline throughout the experiment as the absorption from endogenous absorbers was minimal. The intensity in this wavelength was subtracted from all other wavelengths to derive the corrected PA signal. For the temperature *versus* PA signal plots, all data were normalized to the maximum value of the trace. For the JNP treatment group, all data were globally fitted to a modified 4-parameter logistical curve.

Conflict of Interest: The authors declare no competing financial interest.

Acknowledgment. This work was supported by a grant from the Terry Fox Research Institute, with additional support from the Natural Sciences and Engineering Research Council of Canada, the Canadian Institutes for Health Research, the Ontario Institute for Cancer Research, Prostate Cancer Canada, the Canadian Foundation of Innovation, the Joey and Toby Tanenbaum/Brazilian Ball Chair in Prostate Cancer Research, the Campbell Family Institute for Cancer Research, the Princess Margaret Hospital Foundation and the Ontario Ministry of Health and Long-Term Planning. We thank W. Chan, C. Yip and J. Chen for insightful discussion. Also, M. Lakshman from FUJIFILM VisualSonics, Inc. for technical assistance with the photoacoustic imager.

Supporting Information Available: Characterization of synthesized Bchl-lipid (Figure S1), absorption spectrum of Bchl-lipid dissolved in methanol (Figure S2); absorption spectrum and temperature melt properties of Bchl (15 mol %) inserted in a DPPC nanovesicle (Figure S3); effect of mixing unlabeled DPPC

liposomes with JNP16 (Figure S4); storage stability of JNP in phosphate buffered saline (Figure S5); influence of heating on fluorescence emission spectra and circular dichroism (Figure S6); photoacoustic spectrum of JNP16 above and below phase transition temperature of DPPC (Figure S7); recovery of JNP absorbance after heating, during isothermal conditions (Figure S8); schematic of heating apparatus for *in vivo* JNP experiments (Figure S9); average tissue-water bath temperature differential in control animals during the course of *in vivo* heating experiment (Figure S10); videos corresponding to images in Figure 5 (mp4). This material is available free of charge *via* the Internet at http://pubs.acs.org.

REFERENCES AND NOTES

1. Wang, L. V. Prospects of Photoacoustic Tomography. *Med. Phys.* **2008**, *35*, 5758–5767.
2. Wang, L. V.; Hu, S. Photoacoustic Tomography: *In Vivo* Imaging from Organelles to Organs. *Science* **2012**, *335*, 1458–1462.
3. Cox, B.; Laufer, J. G.; Arridge, S. R.; Beard, P. C. Quantitative Spectroscopic Photoacoustic Imaging: A Review. *J. Biomed. Opt.* **2012**, *17*, 061202(1)–061202(22).
4. Zhang, C.; Maslov, K.; Wang, L. V. Subwavelength-Resolution Label-Free Photoacoustic Microscopy of Optical Absorption in Vivo. *Opt. Lett.* **2010**, *35*, 3195–3197.
5. Zhang, H. F.; Maslov, K.; Stoica, G.; Wang, L. V. Functional Photoacoustic Microscopy for High-Resolution and Noninvasive *in Vivo* Imaging. *Nat. Biotechnol.* **2006**, *24*, 848–851.
6. Allen, T. J.; Hall, A.; Dhillon, A. P.; Owen, J. S.; Beard, P. C. Spectroscopic Photoacoustic Imaging of Lipid-Rich Plaques in the Human Aorta in the 740 to 1400 nm Wavelength Range. *J. Biomed. Opt.* **2012**, *17*, 061209(1)–061209(10).
7. Sethuraman, S.; Amirian, J. H.; Litovsky, S. H.; Smalling, R. W.; Emelianov, S. Y. Spectroscopic Intravascular Photoacoustic Imaging to Differentiate Atherosclerotic Plaques. *Opt. Express* **2008**, *16*, 3362–3367.
8. Wang, X.; Ku, G.; Wegiel, M. A.; Bornhop, D. J.; Stoica, G.; Wang, L. V. Noninvasive Photoacoustic Angiography of Animal Brains *in Vivo* with near-Infraredlight and an Optical Contrast Agent. *Opt. Lett.* **2004**, *29*, 730–732.
9. Agarwal, A.; Huang, S. W.; O'Donnell, M.; Day, K. C.; Day, M.; Kotov, N.; Ashkenazi, S. Targeted Gold Nanorod Contrast Agent for Prostate Cancer Detection by Photoacoustic Imaging. *J. Appl. Phys.* **2007**, *102*, 064701.
10. Lu, W.; Huang, Q.; Ku, G.; Wen, X.; Zhou, M.; Guzatov, D.; Brecht, P.; Su, R.; Oraevsky, A.; Wang, L. V.; *et al.* Photoacoustic Imaging of Living Mouse Brain Vasculature Using Hollow Gold Nanospheres. *Biomaterials* **2010**, *31*, 2617–26.
11. De La Zerda, A.; Zavaleta, C.; Keren, S.; Vaithilingam, S.; Bodapati, S.; Liu, Z.; Levi, J.; Smith, B. R.; Ma, T.-J.; Oralkan, O.; *et al.* Carbon Nanotubes as Photoacoustic Molecular Imaging Agents in Living Mice. *Nat. Nanotechnol.* **2008**, *3*, 557–562.
12. Liu, J.; Geng, J.; Liao, L.-D.; Thakor, N.; Gao, X.; Liu, B. Conjugated Polymer Nanoparticles for Photoacoustic Vascular Imaging. *Polym. Chem.* **2014**, *5*, 2854–2862.
13. Wang, Y.; Zhou, K.; Huang, G.; Hensley, C.; Huang, X.; Ma, X.; Zhao, T.; Sumer, B. D.; DeBerardinis, R. J.; Gao, J. A Nanoparticle-Based Strategy for the Imaging of a Broad Range of Tumours by Nonlinear Amplification of Microenvironment Signals. *Nat. Mater.* **2014**, *13*, 204–212.
14. Dragulescu-Andrasi, A.; Kothapalli, S.-R.; Tikhomirov, G. A.; Rao, J.; Gambhir, S. S. Activatable Oligomerizable Imaging Agents for Photoacoustic Imaging of Furin-like Activity in Living Subjects. *J. Am. Chem. Soc.* **2013**, *135*, 11015–11022.
15. Levi, J.; Kothapalli, S.-R.; Bohndiek, S.; Yoon, J.-K.; Dragulescu-Andrasi, A.; Nielsen, C.; Tisma, A.; Bodapati, S.; Gowrishankar, G.; Yan, X.; *et al.* Molecular Photoacoustic Imaging of Follicular Thyroid Carcinoma. *Clin. Cancer Res.* **2013**, *19*, 1494–1502.
16. Pu, K.; Shuhendler, A. J.; Jokerst, J. V.; Mei, J.; Gambhir, S. S.; Bao, Z.; Rao, J. Semiconducting Polymer Nanoparticles as Photoacoustic Molecular Imaging Probes in Living Mice. *Nat. Nanotechnol.* **2014**, *9*, 233–239.
17. Barone, P. W.; Strano, M. S. Reversible Control of Carbon Nanotube Aggregation for a Glucose Affinity Sensor. *Angew. Chem., Int. Ed.* **2006**, *118*, 8318–8321.
18. Hyun, D. C.; Levinson, N. S.; Jeong, U.; Xia, Y. Emerging Applications of Phase-Change Materials (Pcms): Teaching an Old Dog New Tricks. *Angew. Chem., Int. Ed.* **2014**, *53*, 3780–3795.
19. Sar, A. Form-Stable Paraffin/High Density Polyethylene Composites as Solid−Liquid Phase Change Material for Thermal Energy Storage: Preparation and Thermal Properties. *Energy Convers. Manage.* **2004**, *45*, 2033–2042.
20. Woltman, S. J.; Jay, G. D.; Crawford, G. P. Liquid-Crystal Materials Find a New Order in Biomedical Applications. *Nat. Mater.* **2007**, *6*, 929–938.
21. Alarcon, C. d. l. H.; Pennadam, S.; Alexander, C. Stimuli Responsive Polymers for Biomedical Applications. *Chem. Soc. Rev.* **2005**, *34*, 276–285.
22. Scholes, G. D.; Fleming, G. R.; Olaya-Castro, A.; van Grondelle, R. Lessons from Nature about Solar Light Harvesting. *Nat. Chem.* **2011**, *3*, 763–774.
23. Cogdell, R. J.; Howard, T. D.; Isaacs, N. W.; McLuskey, K.; Gardiner, A. T. Structural Factors Which Control the Position of the Qy Absorption Band of Bacteriochlorophyll a in Purple Bacterial Antenna Complexes. *Photosynth. Res.* **2002**, *74*, 135–141.
24. Scholes, G. D.; Rumbles, G. Excitons in Nanoscale Systems. *Nat. Mater.* **2006**, *5*, 683–696.
25. Eisele, D. M.; Cone, C. W.; Bloemsma, E. A.; Vlaming, S. M.; van der Kwaak, C. G. F.; Silbey, R. J.; Bawendi, M. G.; Knoester, J.; Rabe, J. P.; Vanden Bout, D. A. Utilizing Redox-Chemistry to Elucidate the Nature of Exciton Transitions in Supramolecular Dye Nanotubes. *Nat. Chem.* **2012**, *4*, 655–662.
26. Görl, D.; Zhang, X.; Würthner, F. Molecular Assemblies of Perylene Bisimide Dyes in Water. *Angew. Chem., Int. Ed.* **2012**, *51*, 6328–6348.
27. Jelley, E. E. Spectral Absorption and Fluorescence of Dyes in the Molecular State. *Nature* **1936**, *138*, 2.
28. Jelley, E. E. Molecular, Nematic and Crystal States of I: I-Diethyl-Ψ-Cyanine Chloride. *Nature* **1937**, *139*, 2.
29. Saikin, S. K.; Eisfeld, A.; Valleau, S.; Aspuru-Guzik, A. Photonics Meets Excitonics: Natural and Artificial Molecular Aggregates. *Nanophotonics* **2013**, *2*, 21.
30. Röger, C.; Müller, M. G.; Lysetska, M.; Miloslavina, Y.; Holzwarth, A. R.; Würthner, F. Efficient Energy Transfer from Peripheral Chromophores to the Self-Assembled Zinc Chlorin Rod Antenna: A Bioinspired Light-Harvesting System to Bridge the "Green Gap". *J. Am. Chem. Soc.* **2006**, *128*, 6542–6543.
31. Huber, V.; Katterle, M.; Lysetska, M.; Würthner, F. Reversible Self-Organization of Semisynthetic Zinc Chlorins into Well-Defined Rod Antennae. *Angew. Chem., Int. Ed.* **2005**, *44*, 3147–3151.
32. Isago, H. Spectral Properties of a Novel Antimony(III)-Phthalocyanine Complex That Behaves Like J-Aggregates in Non-Aqueous Media. *Chem. Commun.* **2003**, 1864–1865.
33. Würthner, F.; Thalacker, C.; Diele, S.; Tschierske, C. Fluorescent J-Type Aggregates and Thermotropic Columnar Mesophases of Perylene Bisimide Dyes. *Chemistry* **2001**, *7*, 2245–2253.
34. McDermott, G.; Prince, S. M.; Freer, A. A.; Hawthornthwaite-Lawless, A. M.; Papiz, M. Z.; Cogdell, R. J.; Isaacs, N. W. Crystal Structure of an Integral Membrane Light-Harvesting Complex from Photosynthetic Bacteria. *Nature* **1995**, *374*, 517–521.
35. Reers, M.; Smith, T. W.; Chen, L. B. J-Aggregate Formation of a Carbocyanine as a Quantitative Fluorescent Indicator of Membrane Potential. *Biochemistry* **1991**, *30*, 4480–4486.
36. Kato, N.; Prime, J.; Katagiri, K.; Caruso, F. Preparation of J-Aggregate Liposome Dispersions and Their Chromic Transformation. *Langmuir* **2004**, *20*, 5718–5723.

37. Maiti, N. C.; Mazumdar, S.; Periasamy, N. J- and H-Aggregates of Porphyrin−Surfactant Complexes: Time-Resolved Fluorescence and Other Spectroscopic Studies. *J. Phys. Chem. B* **1998**, *102*, 1528–1538.
38. Andrade, S. M.; Teixeira, R.; Costa, S. M. B.; Sobral, A. J. F. N. Self-Aggregation of Free Base Porphyrins in Aqueous Solution and in Dmpc Vesicles. *Biophys. Chem.* **2008**, *133*, 1–10.
39. Kozyrev, A. N.; Chen, Y.; Goswami, L. N.; Tabaczynski, W. A.; Pandey, R. K. Characterization of Porphyrins, Chlorins, and Bacteriochlorins Formed *via* Allomerization of Bacteriochlorophyll A. Synthesis of Highly Stable Bacteriopurpurinimides and Their Metal Complexes. *J. Org. Chem.* **2006**, *71*, 1949–1960.
40. Lovell, J. F.; Jin, C. S.; Huynh, E.; Jin, H.; Kim, C.; Rubinstein, J. L.; Chan, W. C. W.; Cao, W.; Wang, L. V.; Zheng, G. Porphysome Nanovesicles Generated by Porphyrin Bilayers for Use as Multimodal Biophotonic Contrast Agents. *Nat. Mater.* **2011**, *10*, 324–332.
41. Walczak, P. B.; Eisfeld, A.; Briggs, J. S. Exchange Narrowing of the J Band of Molecular Dye Aggregates. *J. Chem. Phys.* **2008**, *128*, 044505(1)–044505(11).
42. Chen, Y.-S.; Frey, W.; Walker, C.; Aglyamov, S.; Emelianov, S. Sensitivity Enhanced Nanothermal Sensors for Photoacoustic Temperature Mapping. *J. Biophotonics* **2013**, *6*, 534–542.
43. Pramanik, M.; Wang, L. V. Thermoacoustic and Photoacoustic Sensing of Temperature. *J. Biomed. Opt.* **2009**, *14*, 054024(1)–054024(7).
44. Tenchov, B. On the Reversibility of the Phase Transitions in Lipid-Water Systems. *Chem. Phys. Lipids* **1991**, *57*, 165–177.
45. Kim, C.; Cho, E. C.; Chen, J.; Song, K. H.; Au, L.; Favazza, C.; Zhang, Q.; Cobley, C. M.; Gao, F.; Xia, Y.; *et al. In Vivo* Molecular Photoacoustic Tomography of Melanomas Targeted by Bioconjugated Gold Nanocages. *ACS Nano* **2010**, *4*, 4559–4564.
46. Kandulla, J.; Elsner, H.; Birngruber, R.; Brinkmann, R. Noninvasive Optoacoustic Online Retinal Temperature Determination During Continuous-Wave Laser Irradiation. *J. Biomed. Opt.* **2006**, *11*, 041111(1)–041111(3).
47. Larina, I. V.; Larin, K. V.; Esenaliev, R. O. Real-Time Optoacoustic Monitoring of Temperature in Tissues. *J. Phys. D: Appl. Phys.* **2005**, *38*, 2633–2639.
48. Chitnis, P. V.; Mamou, J.; McLaughlan, J.; Murray, T.; Roy, R. A. Photoacoustic Thermometry for Therapeutic Hyperthermia. In *Photoacoustic Thermometry for Therapeutic Hyperthermia*, Ultrasonics Symposium (IUS), 2009, Sept. 20−23, 2009; IEEE International: Piscataway, New Jersey, 2009; pp 1757−1760.
49. Yao, J.; Ke, H.; Tai, S.; Zhou, Y.; Wang, L. V. Absolute Photoacoustic Thermometry in Deep Tissue. *Opt. Lett.* **2013**, *38*, 5228–5231.
50. Prabhakar, U.; Maeda, H.; Jain, R. K.; Sevick-Muraca, E. M.; Zamboni, W.; Farokhzad, O. C.; Barry, S. T.; Gabizon, A.; Grodzinski, P.; Blakey, D. C. Challenges and Key Considerations of the Enhanced Permeability and Retention Effect for Nanomedicine Drug Delivery in Oncology. *Cancer Res.* **2013**, *73*, 2412–2417.
51. Choi, M. J.; Guntur, S. R.; Lee, K. I. L.; Paeng, D. G.; Coleman, A. A Tissue Mimicking Polyacrylamide Hydrogel Phantom for Visualizing Thermal Lesions Generated by High Intensity Focused Ultrasound. *Ultrasound Med. Biol.* **2013**, *39*, 439–448.